Int J Comput Vis (2011) 91: 233–250
DOI 10.1007/s11263-010-0388-9

A Quaternion Framework for Color Image Smoothing and Segmentation

Özlem N. Subakan · Baba C. Vemuri

Received: 3 July 2009 / Accepted: 16 September 2010 / Published online: 18 November 2010

Abstract In this paper, we present feature/detail preserving models for color image smoothing and segmentation using the Hamiltonian quaternion framework. First, we introduce a novel quaternionic Gabor filter (QGF) which can combine the color channels and the orientations in the image plane. We show that these filters are optimally localized both in the spatial and frequency domains and provide a good approximation to quaternionic quadrature filters. Using the QGFs, we extract the local orientation information in the color images. Second, in order to model this derived orientation information, we propose continuous mixtures of appropriate exponential basis functions and derive analytic expressions for these models. These analytic expressions take the form of spatially varying kernels which, when convolved with a color image or the signed distance function of an evolving contour (placed in the color image), yield a detail preserving smoothing and segmentation, respectively. Several examples on widely used image databases are shown to depict the performance of our algorithms.

Keywords Color image smoothing · Color image segmentation · Quaternions · Quaternion Gabor filter · Continuous mixture models · Directional distributions · Watson distribution · von Mises distribution · Matrix-Fisher distribution

This research was in part funded by the NSF grant IOS-0920145.

Ö.N. Subakan · B.C. Vemuri (✉)
Department of Computer and Information Science and Engineering, University of Florida, Gainesville, FL 32611, USA
e-mail: vemuri@cise.ufl.edu

Ö.N. Subakan
e-mail: ons@cise.ufl.edu

1 Introduction

Color conveys essential information that can be employed in many vision tasks including but not limited to object recognition, tracking, segmentation, registration etc. With significant advances in computing power and memory over the past two decades, color image processing has attracted much interest in the recent past. In this area, color image denoising and segmentation are still elusive challenges. Due to the multichannel nature of the color images, the key issue is how to couple the information contained in the given color (e.g. red, green and blue) channels. Considering each individual channel of a color image as a separate monochrome image, the early approaches often involved component-wise application of the traditional gray level techniques on each channel separately. However, this approach fails to capture the inherent correlation between the components and results in color artifacts or blending. To avoid this, color image processing should be performed in a more coherent manner. In order to restore color and other vector-valued images, Blomgren and Chan (1998) proposed to minimize a measure of *Color Total Variation* which is similar to a channel by channel *Total Variation* diffusion, but weighted by a coupling term. To retrieve the local geometry of vector-valued images, Weickert proposed to extend his coherence enhancing diffusion using a common diffusion tensor for all image channels (Weickert 1997). Later, Kimmel et al. introduced a diffusion PDE called *Beltrami flow* (Kimmel et al. 2000) which involves the minimization of the area of the surface representing the vector-valued image with respect to the surface metric. In Tang et al. (2001), authors extended their direction diffusion framework to smoothing only the chromaticity channel of color images, and combined it with the scalar anisotropic diffusion applied to the brightness channel of the color image. In Brook et al. (2003) and Bar

et al. (2007), several extensions of Mumford-Shah functional have been proposed based on a geometric model of images as manifolds, for variational restoration and edge detection in color images. More recently, Tschumperlé introduced an image regularization PDE which takes the curvature constraints into account, and applied it to multi-valued images (Tschumperlé 2006). The non-local (NL) means algorithm of Buades et al. (2005) is considered to be the state-of-the-art in color image denoising. Briefly, NL-means filters are spatially varying filters that replace each pixel value by a non-local average taken over the whole image or in a predefined neighborhood. For more on other multichannel image restoration methods, we refer the reader to Galatsanos et al. (2005) and Lukac et al. (2005).

A vast amount of research has been performed on image segmentation during the past three decades; variational (Mumford and Shah 1985; Paragios et al. 2005), statistical (Geman and Geman 1984; Zhu and Yuille 1996; Cremers et al. 2007), curve evolution based (Kass et al. 1988; Caselles et al. 1993, 1997; Malladi et al. 1995; Kichenassamy et al. 1995; Tsai et al. 2001; Rousson and Paragios 2008), graph-theory based (Boykov et al. 1999; Schoenemann and Cremers 2009) techniques are only some examples. On the other hand, color image segmentation is a relatively nascent area in computer vision. The literature on color image segmentation is not as extensive as that on gray-valued image segmentation. Some published methods directly apply the existing gray level segmentation methods to each channel of a color image and then combine them in some way to obtain a final segmentation result. In the color snakes model (Sapiro 1997), Sapiro extended the geodesic active contour model to the color images based on the idea of evolving the contour with a coupling term based on the eigenvalues of the Riemannian metric of the underlying manifold. Chan et al. extend the Chan-Vese algorithm for scalar-valued images to the vector-valued case (Chan et al. 2000). In their work, in addition to the Mumford-Shah functional over the length of the contour, the minimization involves the sum of the fitting error over each color component. Assuming no correlation between feature channels, Brox et al. propose an energy minimization framework where the energy functional is the sum of the conditional probabilities of the computed features of an image: color channels, optical flow components and texture channels (Brox et al. 2003). In Felzenszwalb and Huttenlocher (2004), color images are handled as three separate monochrome images. In Arbeláez and Cohen (2006), an extension of the Voronoi tessellation to pseudo-metric spaces is applied to color images, where Euclidean distance in Lab color space is used to compute the color differences. Bertelli et al. (2008) present a variational framework based on pairwise pixel similarities; they use L_2 distances in the Lab color space without any coupling between the channels. In Comaniciu and Meer (2002), a mode detection and clustering approach employing the mean shift procedure is presented in the joint spatial-range domain with a Euclidean metric.

In this paper, we adopt a quaternion framework since it offers the scope to process color images holistically, rather than as separate color space components, and thereby handles the coupling between the color channels naturally. Moreover, the trichromatic theory of the human color vision suggests vector mathematics as a natural tool to analyze color images. For a detailed discussion and motivation on the quaternion representation of color images, we refer the reader to Ell and Sangwine (2007) and Moxey et al. (2003). The key innovation of our work here is a unified approach to color image processing using (i) a novel quaternion Gabor filter (QGF) to extract the local orientation, and (ii) continuous mixtures on the unit sphere to model the derived orientation for developing spatially varying smoothing and segmentation kernels.

A major turning point in the field of mathematics, specifically, in algebra, was the birth of the noncommutative algebra via Hamilton's discovery of quaternions in 1843. This discovery was the precursor to new kinds of algebraic structures and has had an impact in various areas of mathematics and physics, including group theory, topology, quantum mechanics etc. In the past few decades, quaternions have been employed in computer graphics (Shoemake 1985), navigation systems (Kuipers 2002) and coding theory (Sethuraman et al. 2003). In computer graphics, quaternion representation of orientations facilitated computationally efficient and mathematically robust (such as avoiding the gimbal lock in Euler angle representation) applications. In image processing, quaternions have been used to represent color images (Pei and Cheng 1996; Sangwine 1996). An image segmentation method that employs quaternionic extension of PCA with the quaternion representation of color has been presented in Shi and Funt (2007). Hui et al. (2006) used standard Gabor filters on color images represented using reduced biquaternions to perform image segmentation. Quaternionic representation of color, together with the extension of the Fourier transform to hypercomplex numbers, has led to applications in color sensitive filtering (Sangwine and Ell 2000a), edge detection (Ell and Sangwine 2007; Sangwine 1998) and cross correlation of color images (Moxey et al. 2003). The very first definition of a hypercomplex Fourier transform was by Delsuc (1988) in nuclear magnetic resonance. Later, different definitions for the quaternionic Fourier transform (QFT) have been introduced in Ell (1993) and Bülow and Sommer (1997a) independently. Based on their definition of QFT, Bülow and Sommer generalized the concept of analytic signal to two dimensions and introduced quaternionic Gabor filters for use with scalar images (Bülow and Sommer 1997b). They extended the Gabor filter by using two quaternion basis i and j to replace the single complex number i in the definition of the complex Gabor filter. However, they did not

consider an application to color images since their definition of QFT associates the imaginary units i and j to the local orientations in the image plane, which has no relationship to the color channels in a color image. In Sangwine and Ell (2000b), an alternative definition for QFT was proposed, which utilizes simple formulae for the Fourier transform of complex-valued signals that can be computed efficiently. We follow this alternative QFT to introduce a novel definition for the Quaternionic Gabor Filters which can be employed to extract features from color images without conflicting interpretations being assigned to the hypercomplex units. We further test QGFs for the optimality with respect to the two-dimensional uncertainty principle. Another contribution of this paper is the formulation of continuous mixture models which incorporate the local orientation, derived using QGFs, into the smoothing and segmentation kernels.

Continuous mixture models have been presented in various contexts (Jian and Vemuri 2007a, 2007b; Jian et al. 2007; Subakan et al. 2007; Subakan and Vemuri 2008). In this paper, we propose continuous mixtures to model the local orientation information extracted via the proposed QGFs. We introduce two such models and derive closed form solutions for the continuous mixture integrals, which are later employed in developing convolution kernels for feature/detail preserving restoration and segmentation of color images. The proposed spatially-varying kernels do not use any prior information, and yet yield high quality results.

The rest of this paper is organized as follows: In Sect. 2, we briefly describe the quaternion algebra and quaternion Fourier transform, and then present a novel definition of the QGFs. In Sect. 3, we introduce a continuous mixture model for quantifying the derived orientation information to perform color image smoothing. In Sect. 4, we propose another continuous mixture model on the derived orientation information for use in segmentation. Section 5 contains the experimental results along with a quantitative evaluation depicting the merits of the proposed approaches, while a summary and an outlook for future research in Sect. 6 conclude the paper.

2 Local Orientation Analysis Using QGFs

Before we delve into the details of this section, a few words on the mathematical notation used in this paper. Throughout the paper, we will use boldface lowercase letters to denote the vectors. Matrices will be denoted by boldface uppercase letters. The ith component of a vector $\mathbf{w}$ is written as w_i, where as $\{\Gamma_i\}_{i=1}^{N}$ denotes the ith Γ matrix in a mixture of size N. $I^v(\cdot)$ denotes the vth component of a vector-valued function $I(\cdot)$.

2.1 Quaternions

In this section, we present background material on quaternions and the associated algebra which will be used in developing the local orientation analysis using QGFs.

Higher dimensional complex numbers are called *hypercomplex* and defined as

$$q = q_0 + \sum_{k=1}^{N} i_k q_k, \quad q_k \in \mathbb{R}, \tag{1}$$

where i_k is orthonormal to i_l for $k \neq l$ in an $N+1$ dimensional space. The Hamiltonian quaternions form a unitary $\mathbb{R}$-algebra; the basic algebraic form for a quaternion $q \in \mathbb{H}$ is:

$$q_0 + q_1 i + q_2 j + q_3 k, \tag{2}$$

where $q_0, q_1, q_2, q_3 \in \mathbb{R}$, the field of real numbers, and i, j, k are three imaginary numbers. $\mathbb{H}$ can be regarded as a 4-dimensional vector space over $\mathbb{R}$ with the natural definition of addition and scalar multiplication. The set $\{1, i, j, k\}$ is a natural basis for this vector space. $\mathbb{H}$ is made into a ring by the usual distributive law together with the following multiplication rules:

$$i^2 = j^2 = -1, \quad ij = -ji = k. \tag{3}$$

If we denote the scalar and vector parts of a quaternion q by $Sq = q_0$ and $Vq = q_1 i + q_2 j + q_3 k$ respectively, the product of two quaternions q and p can be written as

$$qp = SqSp - Vq \cdot Vp + SqVp + SpVq + Vq \times Vp, \tag{4}$$

where the $\cdot$ and $\times$ indicate the vector dot and cross products respectively. The conjugate of a quaternion, denoted by $*$, simply negates the vector part, $q^* = q_0 - q_1 i - q_2 j - q_3 k$. The norm of a quaternion q is $\|q\| = \sqrt{qq^*} = \sqrt{q^*q} = \sqrt{q_0^2 + q_1^2 + q_2^2 + q_3^2}$. A quaternion with unit norm is called *unit quaternion*. Hamilton called a quaternion with zero scalar part a *pure quaternion*. We can give an inner product structure to $\mathbb{H}$ if we define:

$$\langle q, p \rangle = Sqp^*. \tag{5}$$

Using the inner product, the angle α between two quaternions can be defined as:

$$\cos\alpha = \frac{Sqp^*}{\|q\|\|p\|} \tag{6}$$

and

$$d(q, p) = 2\cos^{-1}\big(S(qp^*)\big) \tag{7}$$

is the length of the shortest geodesic between two unit quaternions q and p. It can also be called the *angle of rotation* metric for quaternions. Any quaternion can be written in polar form

$$q = \|q\|e^{\theta\mu} = \|q\|(\cos\theta + \mu\sin\theta), \tag{8}$$

where μ is a unit pure quaternion.

Quaternion representation of color image pixels has been proposed independently in Pei and Cheng (1996) and Sangwine (1996). They encode the color value of each pixel in a pure quaternion. For example, a pixel value at a location (n, m) in an RGB image can be given as a quaternion-valued function $f(n, m) = R(n, m)i + G(n, m)j + B(n, m)k$ where R, G and B denote the red, green and blue components of each pixel respectively. This 3-component vector representation yields a system which has well-defined and well-behaved mathematical operations to apply to color images holistically. An elaborate discussion and motivation for the application of such hypercomplex algebras in signal processing is given in Alfsmann et al. (2007).

2.2 Quaternionic Gabor Filters

In order to develop complex Gabor filters in higher-dimensions, we first need to analyze the corresponding generalization of the Fourier transform. The very first definition of a hypercomplex Fourier transform was due to Delsuc (1988). Later, Ell (1993) and Bülow (1997a) independently introduced the quaternion Fourier transform, respectively as follows:

$$H(jw, kv) = \int_{-\infty}^{\infty}\int_{-\infty}^{\infty} e^{-jwt}h(t, \tau)e^{-kv\tau}\,\mathrm{d}t\,\mathrm{d}\tau, \tag{9}$$

$$F(u, v) = \int_{\mathbb{R}^2} e^{-i2\pi ux} f(x, y)e^{-j2\pi vy}\,\mathrm{d}x\,\mathrm{d}y. \tag{10}$$

In Sangwine and Ell (2000b), another definition for QFT was proposed with the motivation of using a simple generalization of the standard complex operational formulae for convolution in color images:

$$F[u, v] = \frac{1}{\sqrt{MN}}\sum_{m=0}^{M-1}\sum_{n=0}^{N-1} e^{-\mu 2\pi(mv/M+nu/N)} f(n, m), \tag{11}$$

where μ is a unit pure quaternion. In the rest of this paper, we will follow this above definition. For color images in RGB space, μ is chosen as $\frac{1}{\sqrt{3}}(i + j + k)$. Note that both the luminance and the chromaticity information is still preserved; this is still a full color image processing, not a processing of the corresponding gray scale image. The transform operation intrinsically handles the coupling between color channels. First we prove the modulation theorem for the continuous QFT.

Theorem 1 (Modulation theorem for QFT) *Let $f(x, y)$ be a quaternion-valued signal, $F_{\mathbb{H}}(u, v)$ be its quaternion Fourier transform, and $h(x, y) = f(x, y)e^{\mu 2\pi(u_0x+v_0y)}$. Then,* $\mathrm{QFT}\{h(x, y)\} = F_{\mathbb{H}}(u - u_0, v - v_0)$.

Proof

$$\mathrm{QFT}\big\{f(x, y)\big\} = \int_{\mathbb{R}^2} f(x, y)e^{-\mu 2\pi(ux+vy)}\,\mathrm{d}\mathbf{x} =: F_{\mathbb{H}}(u, v),$$

$$\begin{aligned}\mathrm{QFT}\big\{h(x, y)\big\} &= \int_{\mathbb{R}^2} f(x, y)e^{\mu 2\pi(u_0x+v_0y)}e^{-\mu 2\pi(ux+vy)}\,\mathrm{d}\mathbf{x}\\ &= F_{\mathbb{H}}(u - u_0, v - v_0).\end{aligned}$$

□

In the following, we introduce a novel quaternionic Gabor filter.

Definition 1 (Quaternionic Gabor filter) The impulse response of a quaternionic Gabor filter is a Gaussian modulated with the basis functions of the QFT:

$$G_{\mathbb{H}}(\mathbf{x}; \mathbf{u}, \sigma, \lambda, \alpha) = g(x', y')\exp\big(\mu 2\pi(u_0x + v_0y)\big), \tag{12}$$

where $g(x, y) = N\exp(-\frac{x^2+\lambda y^2}{2\sigma^2})$ with N being the normalization constant, λ being the aspect ratio

$$\begin{bmatrix}x'\\ y'\end{bmatrix} = \begin{bmatrix}\cos\alpha & \sin\alpha\\ -\sin\alpha & \cos\alpha\end{bmatrix}\begin{bmatrix}x\\ y\end{bmatrix}.$$

The center frequency of the QGF is given by $\sqrt{u_0^2 + v_0^2}$ and its orientation is $\alpha = \arctan(v_0/u_0)$. Figure 1 depicts a quaternionic Gabor filter with orientation $\pi/4$ for illustration purposes.

Let us consider the QFT of an isotropic Gaussian in $2D$. QFT of an anisotropic Gaussian can be evaluated similarly

$$\begin{aligned}&\mathrm{QFT}\big\{g(x, y)\big\}\\ &= N\int_{\mathbb{R}^2} e^{-\frac{x^2+y^2}{2\sigma^2}}e^{-\mu 2\pi(ux+vy)}\,\mathrm{d}\mathbf{x}\\ &= N\int_{\mathbb{R}}\left(\int_{\mathbb{R}} e^{-(x+2\pi\mu u\sigma^2)/2\sigma^2}\,\mathrm{d}x\right)\\ &\quad\times e^{-\frac{y^2}{2\sigma^2}}e^{\mu^2 2\pi^2\sigma^2u^2}e^{-\mu 2\pi vy}\,\mathrm{d}y\\ &= N_2\int_{\mathbb{R}} e^{-\frac{y^2}{2\sigma^2}}e^{-2\pi^2\sigma^2u^2}e^{-\mu 2\pi vy}\,\mathrm{d}y.\end{aligned} \tag{13}$$

After some algebraic manipulations, we obtain $\mathrm{QFT}\{g(x, y)\} = ce^{-2\pi^2\sigma^2(u^2+v^2)}$, i.e. an un-normalized Gaussian in (u, v)-space, with c being a constant. Hence, using the QFT of a Gaussian together with the modulation theorem for QFT, we can conclude that quaternionic Gabor filters shown above are shifted Gaussian functions in the

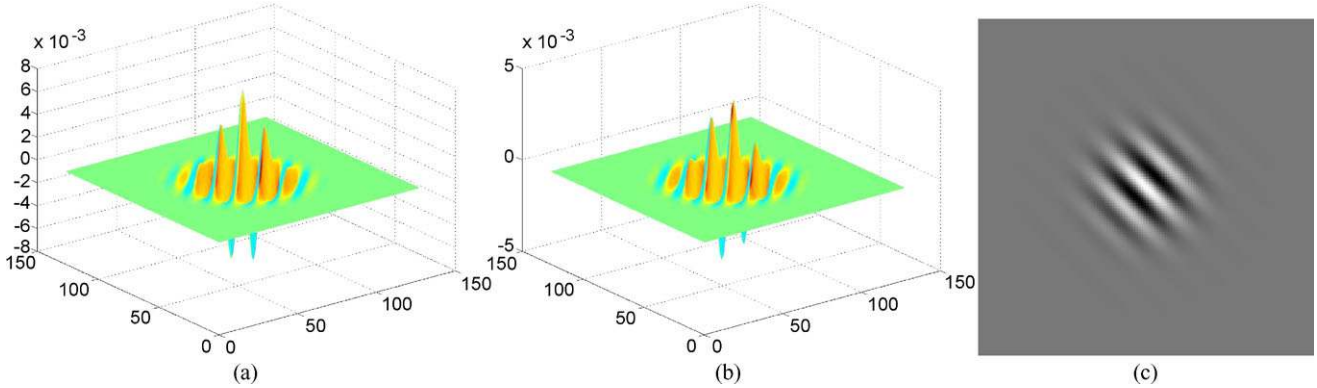

Fig. 1 (Color online) Quaternionic Gabor filter (size of the filter mask is 128×128) with an orientation of $\pi/4$: (**a**) the scalar part of the filter, (**b**) a component of the vector part of the filter, (**c**) 2D view of the scalar part

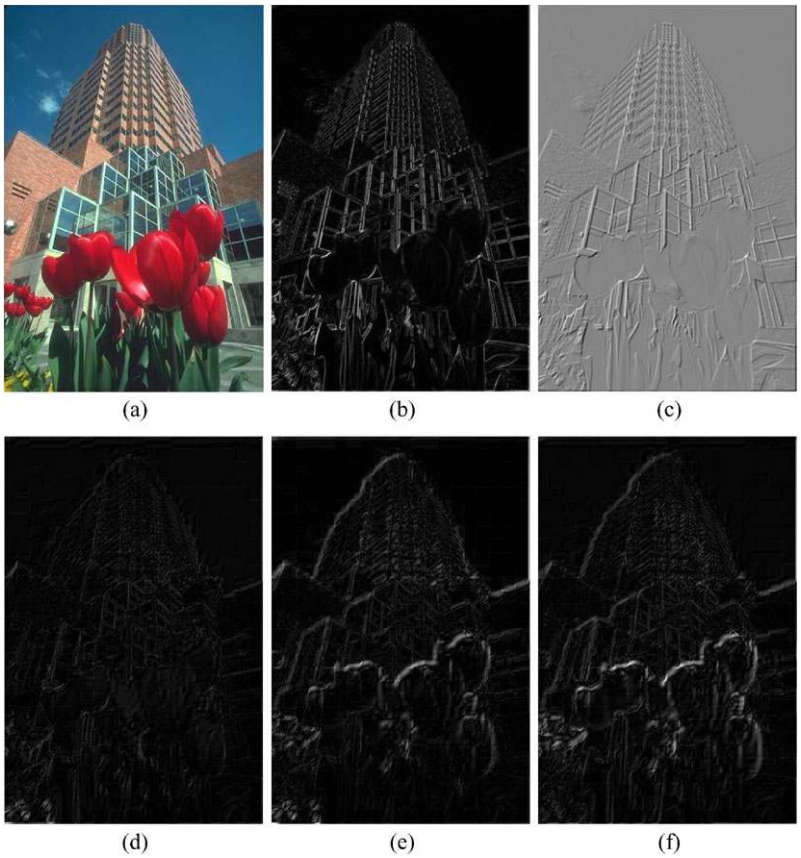

Fig. 2 (Color online) Application of the QGF in Fig. 1 to the image in (**a**) (from Berkeley Data Set—Martin et al. 2001): (**b**) the magnitude response, (**c**)–(**f**) the scalar, i, j, and k parts of the filter response, respectively

quaternionic frequency domain, i.e. if

$$f(\mathbf{x}) = e^{-\frac{x^2}{2\sigma x^2} - \frac{y^2}{2\sigma y^2}} e^{\mu 2\pi (u_0 x + v_0 y)}, \tag{14}$$

then the QFT of f is:

$$F_{\mathbb{H}}(\mathbf{u}) = e^{-2\pi^2 \sigma_x^2 (u-u_0)^2 - 2\pi^2 \sigma_y^2 (v-v_0)^2}. \tag{15}$$

For an application of a QGF, consider the Fig. 2. If we apply the QGF in Fig. 1 to an image, then we obtain high responses wherever there are $\pi/4$ oriented features. Figure 2b illustrates the magnitude response of such a horizontally oriented QGF convolved with an image in quaternion form. Quaternion convolution is equivalently performed by using QFT. Note that all the calculations follow the rules of the quaternion algebra. In this paper, we use the QFT to carry out the convolution operation.

In analogy to Gabor filters, we consider the quaternionic analytic signal which has been defined in Bülow and Sommer (1997b) to work with QGFs. For positive frequencies u_0 and v_0, the main amount of the Gabor filter's energy in

(15) is in the upper right quadrant. Hence, QGFs provide approximation to quaternionic analytic signal. In order to show that QGFs are optimally localized in both quaternionic spatial and frequency domains simultaneously, we will simply extend the definition of the uncertainties for quaternion-valued functions which has also been done in Bülow (1999). The *spatial and frequency uncertainties* Δx and Δu of a quaternion-valued signal f can be given as:

$$(\Delta x)^2 = \frac{\int_{\mathbb{R}^2} f(x,y) f^*(x,y) x^2 \,\mathrm{d}x\,\mathrm{d}y}{\int_{\mathbb{R}^2} f(x,y) f^*(x,y)\,\mathrm{d}x\,\mathrm{d}y},$$
$$(\Delta u)^2 = \frac{\int_{\mathbb{R}^2} F_{\mathbb{H}}(u,v) F^*_{\mathbb{H}}(u,v) u^2 \,\mathrm{d}u\,\mathrm{d}v}{\int_{\mathbb{R}^2} F_{\mathbb{H}}(u,v) F^*_{\mathbb{H}}(u,v)\,\mathrm{d}u\,\mathrm{d}v}. \tag{16}$$

The uncertainties of the QGF given in (14) can be evaluated using the above definitions and their analogs for Δy and Δv to be

$$\Delta x = \frac{\sigma_x}{\sqrt{2}}, \qquad \Delta y = \frac{\sigma_y}{\sqrt{2}},$$
$$\Delta u = \frac{1}{2\sqrt{2}\sigma_x \pi}, \qquad \Delta v = \frac{1}{2\sqrt{2}\sigma_y \pi}. \tag{17}$$

Thus, QGFs are shown to achieve the minimum product of uncertainties defined in Daugman (1985)

$$\Delta x \Delta y \Delta u \Delta v = 1/16\pi^2. \tag{18}$$

In Fig. 3, we show the scalar and vector parts of the sum responses obtained from an application of 13 oriented QGFs

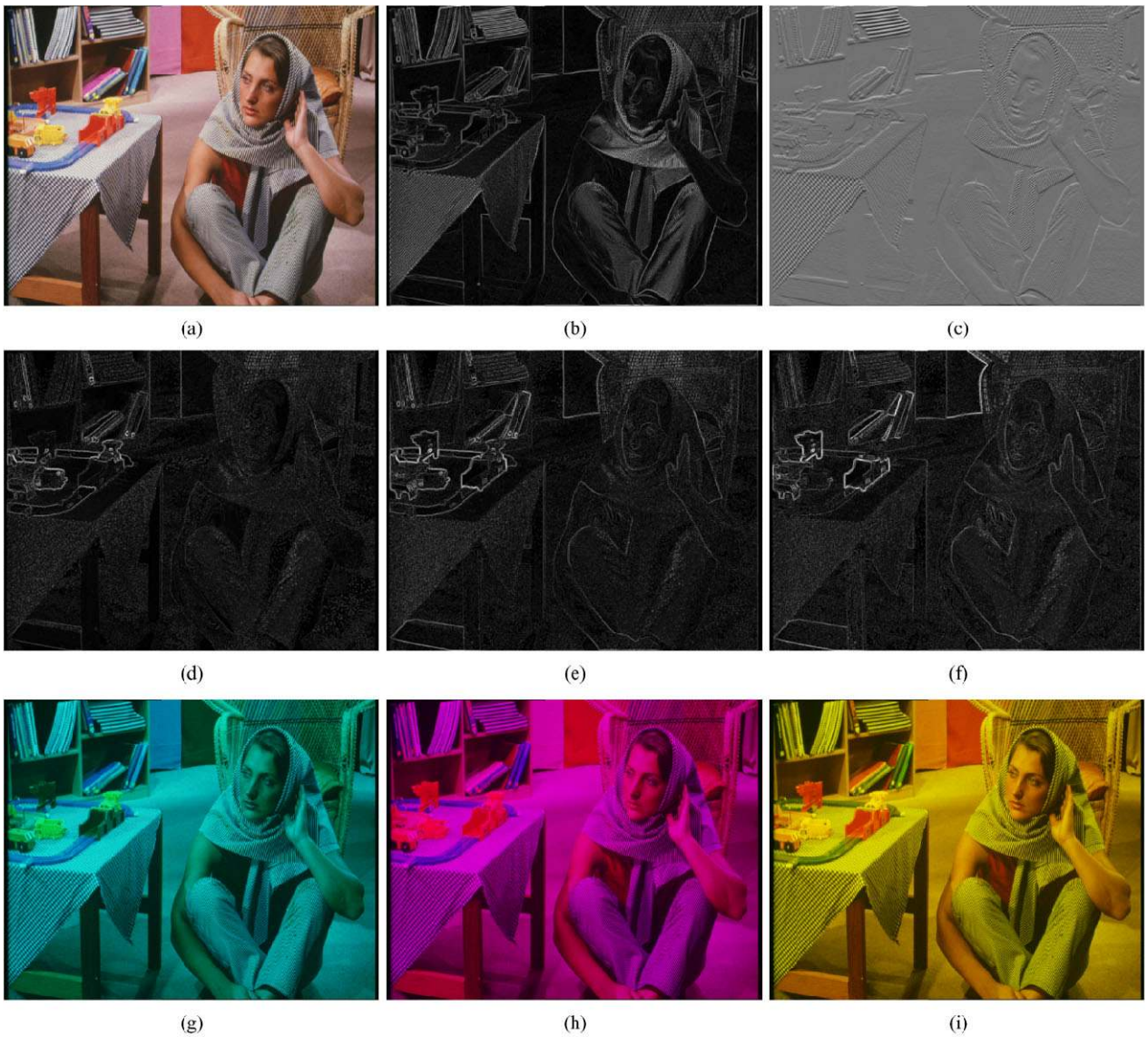

Fig. 3 (Color online) Image of Barbara is quaternion-convolved with QGFs of different orientations. (**a**) *Color image*, (**b**) sum of the magnitude responses, (**c**)–(**f**) scalar, i, j, k parts of the sum of the QGF responses respectively, (**g**)–(**i**) GB, RB, RG images respectively

Fig. 4 (Color online) Application of a quaternionic Gabor filter bank across equal luminance: (**a**) a synthetic color image where the object and the background are of equal luminance, (**b**) luminance channel, (**c**) a grayscale version of (**a**), (**d**) the sum of the magnitude responses of 10 QGFs applied to the *color image* in (**a**)

Fig. 5 (Color online) (**a**) A synthetic *color image* where $(R + G + B)/3$ is the same everywhere. (**b**) $(R + G + B)/3$ values for each pixel. (**c**) The sum of the magnitude responses of the QGFs applied to the *color image* in (**a**)

to the image of Barbara. We convolve the quaternion representation of the color image with each quaternion-valued filter, and then illustrate the sum over each hypercomplex unit. Note that the convolution involves quaternion multiplication. Color transitions in the coupled channels GB, RB and RG show themselves in the components of the vector part of the QGF responses.

In general, in an image, it is possible to have a color contrast without having a luminance contrast. In a black-and-white version of such an image, the two different colored objects appear blended into a single one. In Fig. 4, we demonstrate that the proposed quaternionic Gabor filters can extract the local orientation information from a constant luminance image as well. Figure 4a shows a synthetic color image where all pixels have the same luminance value, but the chromaticity inside the object differs from the chromaticity outside. The luminance channel shows that all pixels have the same value (see Fig. 4b). We applied 10 QGFs to the quaternion representation of this color image. The sum of the magnitude responses of 10 QGFs is shown in Fig. 4d. Although a black-and-white version (Fig. 4c) of the input image is a uniform gray without any changes in orientation, the proposed QGFs successfully derive the orientation information in the color version, showing that they are well suited for analyzing color images and the result is not a grayscale image processing.

The unit pure quaternion direction μ in QGF can be chosen arbitrarily. We have chosen $\mu = \frac{1}{\sqrt{3}}(i + j + k)$, an obvious choice for RGB color images, as it corresponds to the luminance direction on the RGB space. This choice allows treating each color channel equivalently. However, this choice does not mean that the proposed quaternion framework is processing the sum of the RGB values. Also note that the convolution between a QGF and a quaternion representation of a color image is performed following the rules of quaternion algebra. At each pixel, the quaternion-valued filter is multiplied with the color direction of that pixel through a quaternion product. Hence, QGF handles the coupling between the channels while, at the same time, processing all information in a color image. Figure 5a shows a color image where $(R + G + B)/3$ is the same for all pixels. As shown in Fig. 5c, the proposed framework can accurately extract the orientation information.

Note that both the image in Fig. 4 and the image in Fig. 5 cannot be segmented or denoised using a gray-level image processing technique because the objects in the color images do not appear in their gray-valued versions. However, our color image processing framework can detect objects in such images, yielding accurate segmentation and smoothing in the later steps, and this framework is not sensitive to equal luminance.

In the following sections, we present possible ways for modeling the orientation information derived using the QGFs proposed above. We develop two continuous mixture models: in one case, we introduce a model for the components of the quaternion-valued responses, and employ it in color image smoothing, and in the other case we model the magnitude responses to perform detail preserving color image segmentation.

3 A Continuous Mixture on the Orientation Space

In the previous section, we introduced the QGFs to extract the local orientation information in a color image. The resulting responses over a sphere of directions are modeled in this section in a probabilistic framework. We postulate that at each lattice point there is an underlying probability measure induced on the unit circle. An appropriate choice for the basis functions is $\exp(\cos(\theta - \alpha))$, where α is the orientation of the QGF, and θ is a random variable on the circle. The proposed continuous mixture model is given by,

$$G^{v}_{\mathbb{H}}(\mathbf{x}; \cdot, \alpha) = \int_{\mathbb{S}^1} e^{\cos(\theta-\alpha)} \, \mathrm{d}F, \tag{19}$$

where $\mathrm{d}F = f(\theta)\,\mathrm{d}\theta$ denotes the underlying probability measure with respect to the uniform distribution $\mathrm{d}\theta$ on $\mathbb{S}^1$. $G^{v}_{\mathbb{H}}$, $v = i, j, k$ denote the i, j and k components of the vector part in the quaternion-valued response, respectively. We only model the components of the vector part. Scalar part of the filter response can be regarded as a smoothed second derivative of the initial image, and can be used for edge detection.

In order to avoid an ill-posed inverse problem which requires recovering a distribution defined on the circle given the measurements $G^{v}_{\mathbb{H}}(\mathbf{x}; \cdot, \alpha)$, we impose a mixture of von

Mises distributions on θ as a prior. The von Mises distributions have a significant role in statistical inference on the circle, analogous to that of the normal distributions on the line. For statistical purposes, any von Mises distribution can be approximated by a normal distribution wrapped around the circumference of the circle of unit radius. θ is distributed as $f_{\mathcal{M}}(\theta;\beta,\kappa)$ if it has the von Mises density given by,

$$\frac{1}{2\pi\mathcal{I}_0(\kappa)}e^{\kappa\cos(\theta-\beta)}\,\mathrm{d}\theta, \tag{20}$$

where β and κ are the mean direction and the concentration parameter, respectively. $\mathcal{I}_0$ is the modified Bessel function of the first kind and zeroth order (Mardia and Jupp 2000).

This distribution is unimodal and symmetric about $\theta=\beta$. κ determines the degree of the clustering around the mode; the larger the value of κ, the greater the clustering around the mode. In order to handle orientational heterogeneity we need a multimodal distribution. Therefore, we choose the prior to be a discrete mixture of von Mises distributions:

$$\mathrm{d}F=\sum_{n=1}^{N}w_n\frac{1}{2\pi\mathcal{I}_0(\kappa_n)}e^{\kappa_n\cos(\theta-\beta_n)}\,\mathrm{d}\theta. \tag{21}$$

Substituting this measure into (19), we obtain our model given by:

$$G^{v}_{\mathbb{H}}(\mathbf{x};\cdot,\alpha)=\int_{\mathbb{S}^1}\sum_{n=1}^{N}w_n\frac{1}{2\pi\mathcal{I}_0(\kappa_n)}e^{\kappa_n\cos(\theta-\beta_n)}e^{\cos(\theta-\alpha)}\,\mathrm{d}\theta. \tag{22}$$

However, note that this is still a continuous mixture model. N here corresponds to the resolution of the discretization of the circle; it does not correspond to the number of modes (peaks) characterizing the local geometry or the number of dominant local orientations. We observed that the kernel of the von Mises distribution can be utilized to derive a closed form solution for the continuous mixture integral, leading to:

$$G^{v}_{\mathbb{H}}(\mathbf{x};\cdot,\alpha)=\sum_{n=1}^{N}w_n\frac{\mathcal{I}_0(\sqrt{\kappa_n^2+1+2\kappa_n\cos(\beta_n-\alpha)})}{\mathcal{I}_0(\kappa_n)}. \tag{23}$$

We can formulate the computation of this analytic form as the solution to a constrained linear system $\mathsf{A}\mathbf{w}=\mathbf{y}$, where $\mathbf{w}$ is constrained to be non-negative, A is an $M\times N$ matrix with

$$A_{mn}=\frac{\mathcal{I}_0(\sqrt{\kappa_n^2+1+2\kappa_n\cos(\beta_n-\alpha_m)})}{\mathcal{I}_0(\kappa_n)}, \tag{24}$$

$\mathbf{w}=\{w_n\}_{n=1}^{N}$, and $\mathbf{y}=\{G^{v}_{\mathbb{H}}(\mathbf{x};\cdot,\alpha_m)\}_{m=1}^{M}$ contains the measurements obtained via an application of M QGFs to the image, is the unknown weight vector. We solve for the non-negative weights in the mixture using a sparse deconvolution technique, the non-negative least squares (NNLS) minimization (Lawson and Hanson 1974) which yields an accurate and sparse solution for:

$$\min\|\mathsf{A}\mathbf{w}-\mathbf{y}\|^2 \quad \text{subject to} \quad \mathbf{w}\geq 0. \tag{25}$$

A sparse solution is what is expected at each image lattice point since local image geometry does not have a large number of edges meeting at a junction. Once $\mathbf{w}$ is estimated for the given data at each lattice point, we can construct the convolution kernel for color image smoothing. The update equation for image channel I^v, $v=R,G,B$ is given as follows:

$$I^{v}_{t+1}(\mathbf{x})=I^{v}_{t}(\mathbf{x})*Q^{v}(\mathbf{x}),$$
$$Q^{v}(\mathbf{x})=\sum_{n=1}^{N}w^{v}_{n}\frac{\mathcal{I}_0(\sqrt{\kappa_n^2+1+2\kappa_n\cos(\beta_n-\alpha)})}{\mathcal{I}_0(\kappa_n)}, \tag{26}$$

where $Q^v(\mathbf{x})$ is the convolution kernel on the right-hand side of (23) for the corresponding $G^{v}_{\mathbb{H}}(\cdot)$, $\mathbf{w}^v$ is the weight vector obtained from (25) using the corresponding $G^{v}_{\mathbb{H}}(\cdot)$ measurements, β_n is the mean direction of the nth component in the mixture of von Mises distributions, which is obtained by the tessellation of the unit circle, and the orientation α is the angle that the coordinate vector $\mathbf{x}$ makes with the x-axis. M different orientations are employed in a neighborhood of size $\sqrt{M}\times\sqrt{M}$, which yields a kernel of size $\sqrt{M}\times\sqrt{M}$. This formulation yields a spatially varying convolution kernel since the $\mathbf{w}$ vector depends on location; it is estimated at each lattice point $\mathbf{x}$ in an image. Moreover, the weights $\mathbf{w}$ and hence the convolution kernel is different for each color channel I^v. Note that this framework (named as QGvM–Quaternionic Gabor filters with von Mises density) handles the coupling between the color channels through the application of quaternionic Gabor filters to the quaternion representation of the color image, even though the final step involves component-wise convolutions of the computed kernels.

4 A Continuous Mixture on the Unit Quaternion Space

In the previous section, we model the local orientation information in a color image using a continuous mixture model on the unit circle. In this section, we present a model for the magnitude responses on the unit quaternion space. This choice is motivated by the fact that in order to achieve segmentation using an active contour type framework, one

needs to either apply the active contour to some scalar function derived from the input RGB data or represent the data as an image graph, which in this case is a 5 dimensional surface $(x, y, R(x, y), G(x, y), B(x, y))$ and would be computationally expensive. If a channel by channel approach is resorted to, then the segmentations from each channel would have to be somehow combined in a meaningful way to yield a single segmentation, a challenging and hard problem. In this paper, we choose derive the scalar function from the full quaternion representation using the normalized magnitude and then use the space of unit quaternions to construct a continuous mixture model to represent it and solve this integral in closed form for an appropriately chosen prior distribution on this space. This framework is powerful and allows one to capture the complicated local geometries present in the image data and incorporate them into spatially varying segmentation kernels. We postulate that at each lattice point there is an underlying probability measure induced on the manifold of the unit quaternions.

The space of unit quaternions

$$\mathbb{S}^3 = \{q \in \mathbb{H} \mid \|q\| = 1\} \tag{27}$$

is the 3-sphere in $\mathbb{H}$, it forms a group under multiplication and preserves the hermitian inner product. An appropriate choice for the kernel functions is therefore $\exp(-\cos(d(q, p)))$, where $d(q, p) = 2\cos^{-1}(S(q^* p))$ is the length of the geodesic between quaternions q and p, as given in (7). Thus the proposed model is given by,

$$\begin{aligned}&\left\|G_{\mathbb{H}}(\mathbf{x}; \cdot, \alpha)\right\| / G_{\mathbb{H}}^{\max} \\ &\quad = \int_{\mathbb{S}^3} f(q) e^{-\cos(d(q, p_\alpha))}\, \mathrm{d}q,\end{aligned} \tag{28}$$

where $\mathrm{d}F := f(q)\mathrm{d}q$ denotes the underlying probability measure with respect to the uniform distribution $\mathrm{d}q$ on $\mathbb{S}^3$. p_α is the unit quaternion with angle α, which is the orientation of the QGF with respect to the axis $\mu = \frac{1}{\sqrt{3}}(i + j + k)$. $G_{\mathbb{H}}^{\max}$ is the maximal magnitude response among all responses at an image location. In order to avoid an ill-posed inverse problem which requires recovering a distribution defined on the manifold of unit quaternions given the measurements $G_{\mathbb{H}}(\mathbf{x}; \cdot, \alpha)$, we impose a mixture of Bingham distributions on q as a prior. Manifold of the unit quaternions double-covers $SO(3)$. Double-coverage can be interpreted as antipodal-symmetry; thus, Bingham distribution is a natural choice for quaternion priors. For statistical purposes, Bingham distribution is characterized as the hyperspherical analogue of the n-variate normal distribution; essentially it can be obtained by the "intersection" of a zero-mean normal density with the unit sphere in $\mathbb{R}^n$. Let q be a 4-dimensional random unsigned unit direction. q is distributed as $\mathcal{B}_{\mathsf{L},\mathsf{A}}$ if it has the Bingham density (Prentice 1986) given by,

$${}_1F_1(1/2, 2, \mathsf{L})^{-1} \exp\{\operatorname{tr} \mathsf{L}\mathsf{A} q q^T \mathsf{A}^T\}\, \mathrm{d}q, \tag{29}$$

where A is a 4×4 rotation matrix, L is a diagonal matrix with concentration values (which determine the amount of clustering around the mean direction) and ${}_1F_1$ is a confluent hypergeometric function of matrix argument as defined in Herz (1955).

Here, we make a useful observation which helps deriving an analytic solution for the proposed continuous model: Using the relationship between $\mathbb{S}^3$ and $SO(3)$, Prentice (1986) has shown that q has a Bingham density if and only if the corresponding rotation matrix, Q, in $SO(3)$ has a matrix Fisher distribution. A random 3×3 rotation matrix Q is said to have a matrix Fisher distribution $\mathcal{F}_{\mathsf{F}}$ if it has the following pdf:

$${}_0F_1\big(3/2; \mathsf{F}\mathsf{F}^T/4\big)^{-1} \exp\{\operatorname{tr} \mathsf{F}^T \mathsf{Q}\}\, \mathrm{d}\mathsf{Q}. \tag{30}$$

F is a 3×3 parameter matrix which encapsulates the concentration values and orientations, ${}_0F_1$ is a hypergeometric function of matrix argument and can be evaluated using zonal polynomials. By using the distance on the manifold $SO(3)$, the proposed model can be equivalently written in $SO(3)$ instead of $\mathbb{S}^3$ as:

$$\left\|G_{\mathbb{H}}(\mathbf{x}; \cdot, \mathsf{P}_\alpha)\right\| / G_{\mathbb{H}}^{\max} = \int_{SO(3)} e^{-\frac{\operatorname{tr} \mathsf{P}_\alpha^T \mathsf{Q} - 1}{2}}\, \mathrm{d}F, \tag{31}$$

where P_α is the rotation matrix corresponding to the unit quaternion with the angle being the orientation α of the QGF and the axis being $\mu = \frac{1}{\sqrt{3}}(i + j + k)$.

$$\mathrm{d}F = \sum_{i=1}^{N} w_i {}_0F_1\big(3/2; \mathsf{F}_i \mathsf{F}_i^T/4\big)^{-1} e^{\operatorname{tr} \mathsf{F}_i^T \mathsf{Q}}\, \mathrm{d}\mathsf{Q} \tag{32}$$

is a discrete mixture of matrix Fisher densities over the rotation matrix Q with respect to the uniform distribution on $SO(3)$. We choose to change the prior to this mixture of matrix Fisher densities since the matrix Fisher density is unimodal and will not be able to handle orientational heterogeneity. Once again, the model in (31) is still a continuous mixture model. N here corresponds to the resolution of the $SO(3)$ discretization and not the number of dominant local orientations. We observed that the kernel of the matrix Fisher distribution can be utilized to derive a closed form solution for the right-hand side, leading to:

$$\sum_{i=1}^{N} w_i \frac{{}_0F_1\big(\frac{3}{2}; \frac{1}{4}[\mathsf{F}_i - \frac{\mathsf{P}_\alpha}{2}][\mathsf{F}_i - \frac{\mathsf{P}_\alpha}{2}]^T\big)}{{}_0F_1(3/2; \mathsf{F}_i \mathsf{F}_i^T/4)}. \tag{33}$$

In order to compute this analytic form, we can write it as the solution to a linear system $\mathsf{A}\mathbf{w} = \mathbf{y}$ (as in Sect. 3), where $\mathbf{y} = \{\|G_{\mathbb{H}}(\mathbf{x}; \cdot, \alpha_j)\|\}_{j=1}^{M} / G_{\mathbb{H}}^{\max}$ contains the normalized measurements obtained via an application of M QGFs

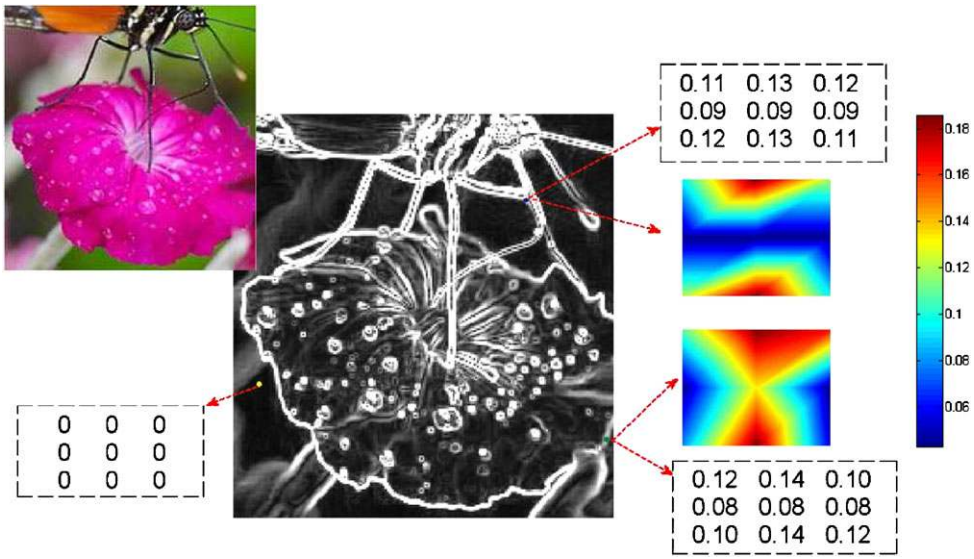

Fig. 6 (Color online) Convolution kernels on a *color image*. Numerical values of the convolution kernels for three locations with different orientational heterogeneity are shown in the figure together with a visual illustration

to the color image, A is an $M \times N$ matrix with

$$A_{ji} = \frac{{}_0F_1(\frac{3}{2}; \frac{1}{4}[\mathsf{F}_i - \frac{P_j}{2}][\mathsf{F}_i - \frac{P_j}{2}]^T)}{{}_0F_1(3/2; \mathsf{F}_i\mathsf{F}_i^T/4)} \tag{34}$$

and $\mathbf{w} = (w_i)$ is the unknown weight vector. The weights in the mixture can be solved using a sparse deconvolution technique, a non-negative least squares (NNLS) minimization which yields an accurate and sparse solution. Once $\mathbf{w}$ is estimated for the given data at each lattice point, we can construct the convolution kernel for color image segmentation. Figure 6 illustrates the 3×3 convolution kernels for different locations in a real image. We represent an evolving curve C (in a curve evolution framework) by the zero level set of a Lipschitz continuous function $\phi : \Omega \to \mathbb{R}$. So, $C = \{(x, y) \in \Omega\colon\ \phi(x, y) = 0\}$. We choose ϕ to be negative inside C and positive outside. C is evolved using the following update equation:

$$\phi_{t+1}(\mathbf{x}) = \phi_t(\mathbf{x}) * K(\mathbf{x}), \tag{35}$$

where $K(\mathbf{x})$ is the convolution kernel obtained from (33) by setting the matrix P to the rotation matrix corresponding to the angle that the coordinate vector $\mathbf{x}$ makes with the x-axis. Note that this formulation (named as QGmF–Quaternionic Gabors with matrix Fisher density) yields a spatially varying convolution kernel since the $\mathbf{w}$ vector is estimated at each lattice point in an image.

5 Experiments and Comparisons

5.1 Experiments on Color Image Smoothing

In this section, we evaluate the performance of the QGvM framework with applications on color image denoising and inpainting. We compare our denoising results with four prominent techniques: Weickert's coherence enhancing diffusion (CED) for color images (Weickert 1997), the Beltrami flow proposed by Kimmel et al. (2000), the curvature preserving regularization (CPR) proposed by Tschumperlé (2006) and the NL-means algorithm Buades et al. (2005) which is considered to be the state-of-the-art in denoising techniques. In the denoising experiments, for each algorithm the outputs that have the highest PSNR values are shown. Parameters of each method were chosen so as to reach its best PSNR value. We compute the PSNR on the RGB channels of the color image. We also report the PSNR values on the luminance channel of the YCbCr representation of the RGB image, since the human eye is more sensitive to the luma information in a color image. PSNR for RGB domain is defined as:

$$\text{PSNR} = 10\log_{10}\frac{255^2}{\text{MSE}} \tag{36}$$
$$\text{MSE} = \frac{1}{3|\Omega|}\sum_{x\in\Omega}\sum_{v=R,G,B}\left(I_0^v(x) - \hat{I}^v(x)\right)^2,$$

where Ω is the image domain of $|\Omega|$ pixels, I_0 is the noise-free ideal image, and $\hat{I}$ is its estimate obtained from the denoising method. PSNR for the luminance channel is the same except the MSE is the sum over the squared value differences of the luminance channel, divided by $|\Omega|$.

In all of our experiments, we use the same number of measurements for our model; i.e. the size of the quaternion Gabor filter bank, M, is 21 for all experiments. N, the resolution of the discretization of the unit circle for the mixing density, is set to 81. Hence, the size of matrix A is 21×81, and the unknown of this under-determined system, which is the weight vector $\mathbf{w}$, is an 81-dimensional vector. Note that

Table 1 The PSNRs of the denoised color images for different algorithms

Image	PSNR method	CED	Beltrami	CPR	NLM	Ours	Noisy image
Butterfly	Luminance	26.45	27.37	25.14	28.4	28.2	22.32
	RGB	24.48	24.84	23.11	26.07	26.33	17.71
Parrots	Luminance	29.01	28.95	28.91	32.62	30.03	22.30
	RGB	26.95	26.85	26.75	29.5	27.70	17.62
Mandrill	Luminance	25.18	25.33	25.43	26.56	27.20	21.63
	RGB	22.53	22.52	22.27	24.26	23.51	19.28
Clown	Luminance	27.79	28.74	30.12	28.54	31.5	22.92
	RGB	25.45	26.28	27.25	26.02	27.68	18.37
Barbara	Luminance	27.81	29.35	30.83	31.56	31.4	22.33
	RGB	24.50	25.20	25.10	25.5	25.30	17.59
Horses	Luminance	27.7	28.04	28.17	28.56	29.21	21.83
	RGB	26.04	26.32	26.29	26.5	27.73	20.20
Peppers	Luminance	31.0	30.57	30.65	31.74	32.47	22.04
	RGB	27.95	27.08	27.20	27.8	28.28	20.06

this size does not correspond to the expected number of different orientations at a pixel. The concentration parameter κ is the same for all distributions in the mixture of von Mises distributions. We experimented with different values of κ and in the following experiments, a value of 8, which gives a relatively sharp mode in a von Mises distribution, yields the best PSNR values. In denoising experiments, the original images are corrupted by additive white-Gaussian noise, having a high standard deviation ($\sigma = 35$). For a quantitative evaluation of our approach, we present the highest PSNR values obtained using the above mentioned methods in Table 1. In all the cases, our unsupervised and adaptive method produces either the best PSNR values or comparable PSNR values to those from NL-means. On a PC with 2.00 GHz CPU and 2 GB RAM, each of our experiments in the following data set runs in about 3 mins. Overall, in the experiments reported in Table 1, our method performs best in 4 out of the 7 cases and is competitive to NL-means in the remaining cases. Also, it is computationally more attractive than NL-means which takes several hours of processing time on the images used in this paper. Moreover, our filters are very well suited for a GPU implementation due to their local nature. We should however note that attempts to make the NL-means algorithm faster is an active area of research.

In Fig. 7, we illustrate the potential of our approach with a butterfly image corrupted by additive white-Gaussian noise, having a high standard deviation (Fig. 7a, $\sigma = 35$). Our method preserves significant geometric features and the original color contrasts without producing undesirable artifacts (see Fig. 7f). However, both in Figs. 7b and 7c, we notice the color artifacts in flat regions, which look like artificial texture effects. Coherence enhancing diffusion creates fiber effects on the background. Curvature preserving regularization performs better, however it creates a color bleeding around the edges of the wings (see zoomed-in view in Fig. 7d). Both visually and in terms of PSNR, our method outperforms the competing methods. NL-means however is quite competitive with our method but due to its global nature, is computationally very slow and takes several hours and is not competitive with respect to ours in this context.

In inpainting, we compare our results with the direct application of the curvature preserving PDE as proposed by Tschumperlé in Tschumperlé (2006), where the regions to be inpainted are removed by the user using a rough mask. To fill-in the missing image regions, we apply the iterative convolution of our spatially-varying kernel on the regions to inpaint, without using any texture synthesis or reconstruction technique as a post-processing step. The coefficients of the spatially varying kernel are estimated as in the case of any image without such an occluded region. The estimated kernels are then applied iteratively without any further changes to the estimated kernels. We illustrate how our technique can be used to remove objects from digital photographs along with the comparisons. In Fig. 8, we would like to remove the net from the image, and in Fig. 9, we would like to take the cage out and fill-in the missing parts. In both experiments, our method generates a better result. Note that the fish net is still noticeable in Fig. 8b, similarly the cage in Fig. 9b. In addition, parrot's toe is over-diffused by the curvature preserving regularization, whereas our result looks visually more appealing.

5.2 Experiments on Color Image Segmentation

In this section, we present several experimental results of our color image segmentation approach QGmF and quanti-

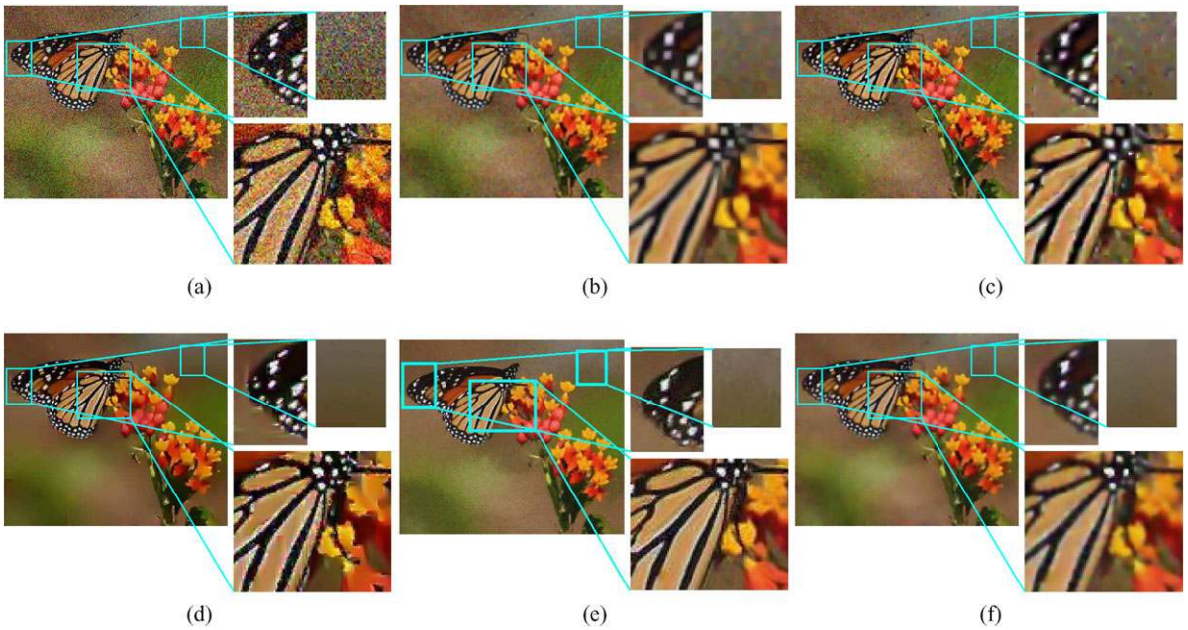

Fig. 7 (Color online) (**a**) Noisy image with a Gaussian noise of standard deviation 35. Denoised images using (**b**) the coherence enhancing diffusion, (**c**) the Beltrami flow, (**d**) the curvature preserving regularization, (**e**) the non-local means and (**f**) our method

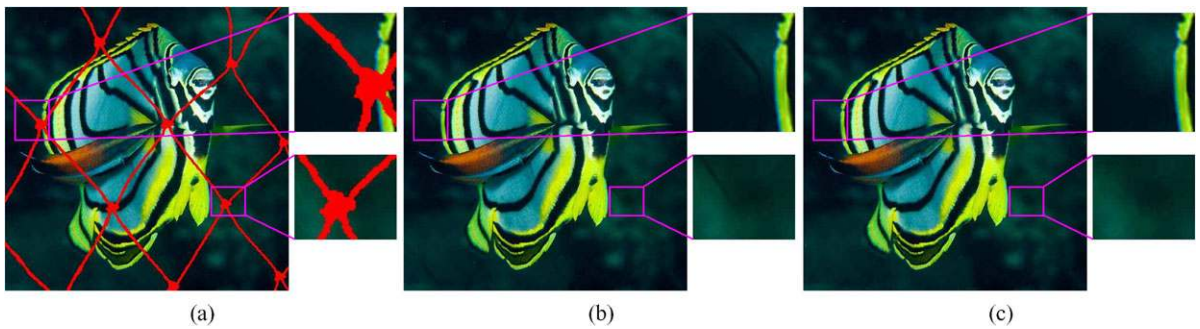

Fig. 8 (Color online) Inpainting a fish net in a *color image* using (**b**) curvature preserving regularization, (**c**) our method

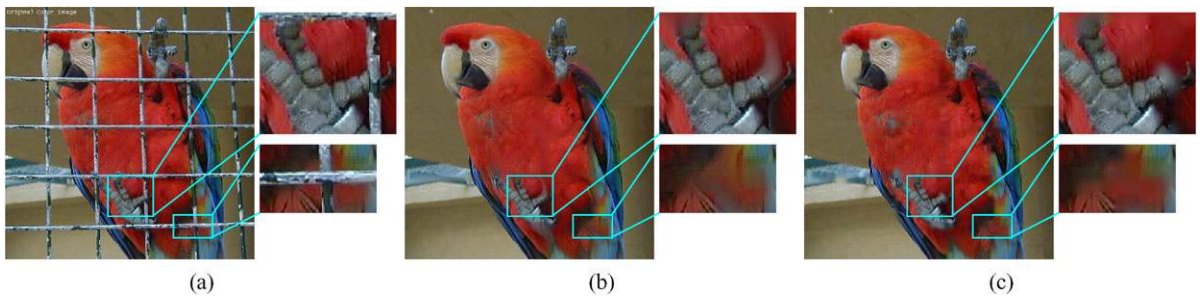

Fig. 9 (Color online) Inpainting a cage in (**a**) a *color image* (courtesy of Tschumperlé 2008), with curvature preserving regularization (**b**), and with our method (**c**)

tatively compare its performance with a state-of-the-art technique in segmentation: the mean shift algorithm presented in Comaniciu and Meer (2002). We compare with this algorithm since it presents a tool for feature-space analysis, and it is publicly available. In this quantitative evaluation, we show the segmentations that yield the highest F-measure value for each algorithm, and present the numerical results in Table 2.

In Fig. 10, we show segmentation results obtained by various recent methods. Our model yields a segmentation

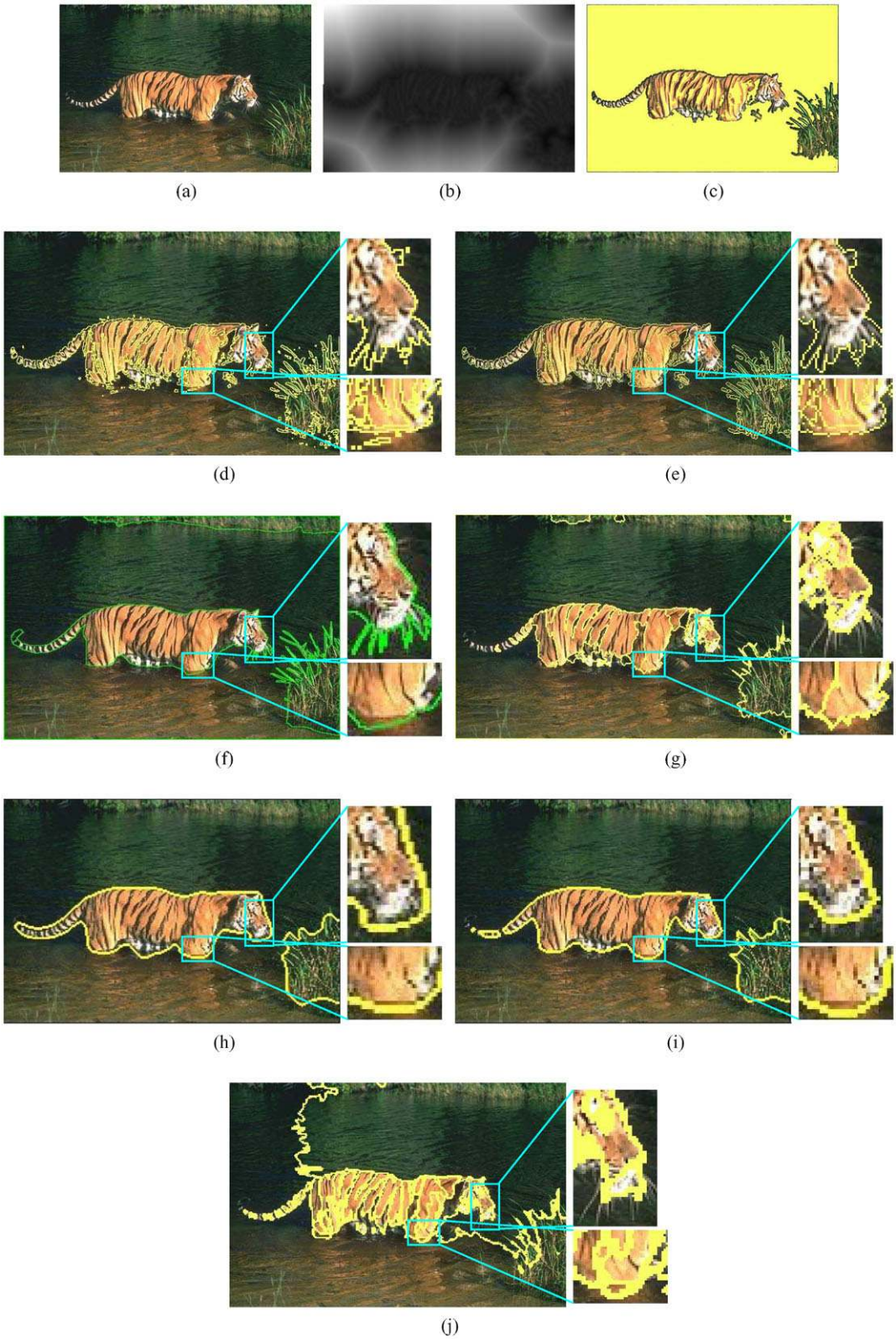

Fig. 10 (Color online) (**a**) Original image. (**b**) Final distance function obtained by QGmF method. (**c**) Regions extracted by the QGmF method. Results obtained from (**d**) the QGmF method with a low threshold value of 0.01. (**e**) The QGmF method with a threshold value of 0.02. (**f**) A human segmentation (from the ground truth in the Berkeley Segmentation Data Set Martin et al. 2001). (**g**) The mean shift algorithm. (**h**) The cue integration method in Brox et al. (2003) using only Gabor features. (**i**) The cue integration method in Brox et al. (2003) using the texture features obtained by structure tensor and the color channels. (**j**) The ultrametric contour map algorithm in Arbeláez and Cohen (2006)

significantly close to the ground truth manual segmentation in the Berkeley database. The zoomed-in views both in Figs. 10d and 10e show the detailed segmentation of the fur under the chin. Also, most of the other methods fail to capture the tail accurately; although Fig. 10i has almost all of the tail segmented, many junctions, edges are not preserved in the segmentation.

In the QGmF, we can adjust the level of details/features, which reveal themselves in the output of the QGF applied to the color images. To do this, we introduce a threshold parameter on the magnitude of the filter responses. A relatively low threshold results in a segmentation capturing the low contrast details in small scales. Figure 11c illustrates such an example where the threshold is set to 0.005. Mean shift algorithm achieves a successful result as shown in Fig. 11b. However, uniform regions are not consistently preserved, e.g.the sky is mis-segmented; the boundaries divide the regions which are actually composed of connected components, as can be seen between the clouds. Moreover, the crowd on parade is mis-segmented with the ground. Figure 11d shows a better segmentation using our QGmF method (note that the man riding the horse and the crowd are clearly segmented, also note the accurate localization of the boundary between the barricade and the pavement). Figure 11e shows the pixels correctly labeled as belonging to the segmentation boundary by the QGmF.

Another visual comparison is provided in Fig. 12. Since the mode detection calculations in the mean shift algorithm are determined by global bandwidth parameters, the algorithm tends to miss small-scale details in some places or over-segment the uniform regions (see the small areas on the starfish which are mis-segmented as being a part of the outer region in Fig. 12b). On the other hand, QGmF maintains coherence within textured regions while preserving the small scale details around the boundaries as shown in Fig. 12d. Once again, a low threshold value results in over-segmentation (see Fig. 12c).

In Fig. 13b, note the regions which have almost equal luminance but different chromaticity. Both Figs. 13c and 13d are over-segmented; however, Fig. 13e shows a high quality result which is very close to the ground truth manual segmentation (see Figs. 13e and 13a). In Fig. 14b, the mean shift segmentation algorithm mis-segments the heads of the astronauts, and the boundaries of the astronaut on the left are missed. As visually evident, QGmF performs better than the competing methods.

In order to have a quantitative evaluation of our approach, we present the highest F_1-measure (or Dice's Coefficient) scores of our method and the competing method for the above images, as shown in Table 2. Furthermore, in Fig. 15

Table 2 F_1-measure (or Dice's coefficient) values for segmented images

Image	QGmF	MeanShift
Astronauts	0.74	0.56
Starfish	0.81	0.52
Parade	0.76	0.65
Buffalo	0.86	0.67
Tiger	0.83	0.64

Fig. 11 (Color online) (**a**) Segmentation performed by a human subject (from the ground truth in the Berkeley Segmentation Data Set, Martin et al. 2001). (**b**) Segmentation result of the mean shift algorithm. (**c**) Segmentation result of the QGmF method with a low threshold value of 0.005. (**d**) Segmentation result of the QGmF method with a threshold value of 0.02. (**e**) True positives (TP) map of (**d**) with respect to (**a**)

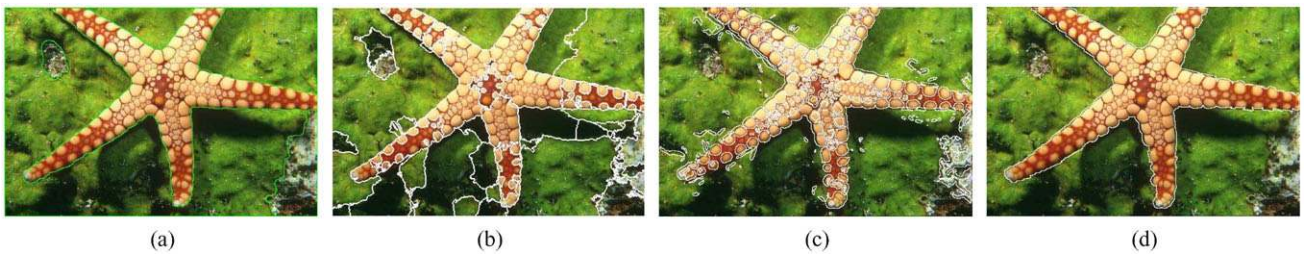

Fig. 12 (Color online) (**a**) Human segmentation (from the ground truth in the Berkeley Segmentation Data Set). (**b**) Output of the mean shift algorithm. (**c**) Output of the QGmF method with a threshold of 0.005. (**d**) Output of the QGmF method with a threshold of 0.025

(a) (b) (c) (d) (e)

Fig. 13 (Color online) (**a**) Human segmentation (from the ground truth data). (**b**) Luminance channel of the color image. (**c**) Output of the QGmF method for the color image (QGF threshold = 0.005). (**d**) Output of the mean shift segmentation. (**e**) Output of the QGmF method (QGF threshold = 0.025)

(a) (b) (c)

Fig. 14 (Color online) (**a**) Manual segmentation (from the ground truth in Berkeley Segmentation Data Set). (**b**) Output of the mean shift segmentation. (**c**) Output of the QGmF method

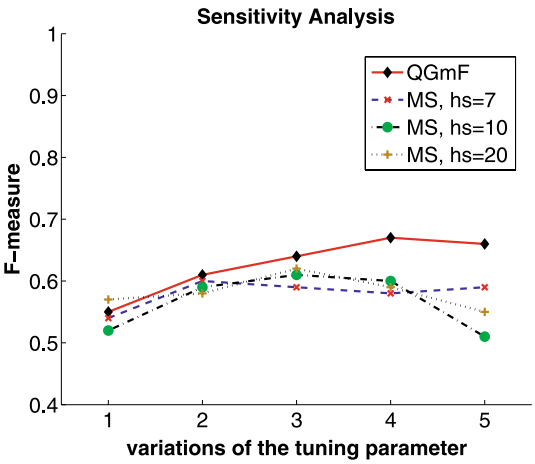

Fig. 15 (Color online) F-measure plots for the mean shift segmentation algorithm and the QGmF convolution-based kernel method on 100 color images from the Berkeley Segmentation Data Set. For the QGmF, x-axis shows the variations of the threshold parameter for QGF responses, arranged in ascending order *from left to right*, while y-axis shows the corresponding F-measure value. The threshold for QGF varies within [0.005, 0.05]. For the mean shift segmentation algorithm, the corresponding values for the space bandwidth parameter (h_s) are shown in the plot, *points along each curve* correspond to the variations of the range bandwidth parameter (h_r) in [4, 20]

we present a sensitivity analysis using the F_1-measures on 100 color images (including the images above) drawn from the Berkeley Segmentation Data Set (Martin et al. 2001). F_1-measure, commonly known as the F-measure, is the evenly weighted harmonic mean of the precision and recall scores. Precision and recall are preferred as measures of the segmentation quality because they are sensitive to under and over-segmentation. The human segmentations from the Berkeley Segmentation Data Set were used as the ground truth in the evaluation. Since there are multiple human segmentations per image, we compute the F-measure scores against each of these segmentations and then take the average. The boundaries between two segmentations are matched by examining a neighborhood within a radius of $\epsilon = 2$. In these experiments, the obtained segmentations are reasonable from the human being perception.

In the QGmF, we tested the effect of the threshold parameter (for values in [0.005, 0.05]) on the QGF responses. For the mean shift segmentation algorithm, we tested the effect of the kernel bandwidth parameters: h_s, space bandwidth; and h_r, range bandwidth. They determine the resolution of the mode selection and the clustering. We tested for 3 different h_s values in [7, 10, 20]. In each curve for the mean shift algorithm, x-axis shows the variations of the h_r values in [4, 20] arranged in ascending order from left to right. Experimentation showed that the F-measure scores change significantly with respect to the bandwidth parameters in mean shift segmentation algorithm, making it difficult to choose the range of the parameters which can provide good results. In the QGmF, we observed that a low threshold value for QGF results in over-segmentation which is characterized in the curves by low F-measure, whereas any level of detail for segmentation can be achieved by tuning the threshold parameter. We notice that the scores of the QGmF are higher than the competing method.

6 Conclusion

In this paper, we presented quaternion-based frameworks for feature/detail preserving restoration and segmentation in color images. The main idea is to capture the complicated local geometry contained at a lattice point, and then to incorporate this information into spatially varying convolution filters. We first introduced a novel quaternionic Gabor filter to extract the local orientation information while appreciating the vectorial nature of a color image. We explored different continuous mixture models in order to convey the derived quaternion-valued orientation information to color smoothing and segmentation. One of the proposed models represents each component of the quaternion-valued QGF responses using a continuous mixture model on the orientation space, which is the unit circle. The other quantifies the magnitude data of the QGF responses via a continuous mixture of hypercomplex exponential basis functions on the unit quaternion space. Deriving analytic solutions for these integrals, we developed spatially varying convolution kernels. Our methods do not use any prior information. We qualitatively and quantitatively validated that our frameworks deliver superior or competitive (with respect to the non-local means in the denoising case) performance in comparison to competing state-of-the-art methods.

The proposed methods handle the coupling between the channels through the application of QGFs to the quaternion representation of color images. This process also integrates the color information and the texture information. In segmentation, the active contour evolution is controlled by this unified information. Similarly, in the denoising task, image channels do not evolve independently because the orientation space and the color components are linked through the QGFs. For color image smoothing, we envision that the update equation of the smoothing process can be modified to perform a quaternion-convolution of color image with a quaternion-valued kernel. Another possible research direction involves exploring the ways to model the full quaternion-valued QGF response using quaternion-valued basis functions together with the distributions on the unit quaternion space. This may be accompanied with extensions of the sparse deconvolution techniques to hypercomplex systems. Our future research will entail the search for such formulations to discover new and valuable tools for color image processing.

Acknowledgements Authors like to express their thanks to, Ajit Rajwade for helping with some of the experiments reported here and Dr. Angelos Barmpoutis for his help in revising the manuscript. Some of the color image data was taken from the Computer Vision text book by Jain, Kasturi and Schunk and the rest was taken from the UC Berkeley image data base.

Appendix

In this appendix we provide the matrix version of the quaternion Fourier transform in (11) in order to show the explicit interactions between the red, green and blue channels (R, G, B) in a color image represented in the quaternion from. Given a field of quaternions $f(n,m) = S_{n,m} + R_{n,m}i + G_{n,m}j + B_{n,m}k$, its QFT (11) is given by

$$\begin{pmatrix} S_{u,v} \\ R_{u,v} \\ G_{u,v} \\ B_{u,v} \end{pmatrix} = \frac{1}{\sqrt{3MN}} \sum_{m=0}^{M-1} \sum_{n=0}^{N-1} \mathbf{A} \begin{pmatrix} S_{n,m} \\ R_{n,m} \\ G_{n,m} \\ B_{n,m} \end{pmatrix} \tag{37}$$

where

$$\mathbf{A} = \begin{pmatrix} \sqrt{(3)}\cos(\phi) & -\sin(\phi) & -\sin(\phi) & -\sin(\phi) \\ \sin(\phi) & \sqrt{(3)}\cos(\phi) & -\sin(\phi) & \sin(\phi) \\ \sin(\phi) & \sin(\phi) & \sqrt{(3)}\cos(\phi) & -\sin(\phi) \\ \sin(\phi) & -\sin(\phi) & \sin(\phi) & \sqrt{(3)}\cos(\phi) \end{pmatrix}$$

and $\phi = -2\pi(mv/M + nu/N)$. We should note that (37) was derived from (11) by using quaternion multiplication as presented in Sect. 2.1.

References

Alfsmann, D., Göckler, H. G., Sangwine, S. J., & Ell, T. A. (2007). Hypercomplex algebras in digital signal processing: benefits and drawbacks (tutorial). In *EURASIP 15th European signal processing conference, EUSIPCO 2007*, Poland (pp. 1322–1326).

Arbeláez, P. A., & Cohen, L. D. (2006). A metric approach to vector-valued image segmentation. *International Journal of Computer Vision*, *69*(1), 119–126.

Bar, L., Brook, A., Sochen, N., & Kiryati, N. (2007). Deblurring of color images corrupted by impulsive noise. *IEEE Transactions on Image Processing*, *16*(4), 1101–1111.

Bertelli, L., Sumengen, B., Manjunath, B., & Gibou, F. (2008). A variational framework for multiregion pairwise-similarity-based image segmentation. *IEEE Transactions on Pattern Analysis and Machine Intelligence*, *30*(8), 1400–1414.

Blomgren, P., & Chan, T. F. (1998). Color TV: total variation methods for restoration of vector-valued images. *IEEE Transactions on Image Processing*, *7*(3), 304–309.

Boykov, Y., Veksler, O., & Zabih, R. (1999). Fast approximate energy minimization via graph cuts. *IEEE Transactions on Pattern Analysis and Machine Intelligence*, *23*(2001), 1222–1239.

Brook, A., Kimmel, R., & Sochen, N. A. (2003). Variational restoration and edge detection for color images. *Journal of Mathematical Imaging and Vision*, *18*(3), 247–268.

Brox, T., Rousson, M., Deriche, R., & Weickert, J. (2003). Unsupervised segmentation incorporating colour, texture, and motion. In *Computer analysis of images and patterns* (pp. 353–360).

Buades, A., Coll, B., & Morel, J. M. (2005). A non-local algorithm for image denoising. In *IEEE computer vision and pattern recognition, CVPR* (Vol. 2, pp. 60–65). Los Alamitos: IEEE Comput. Soc.

Bülow, T. (1999). *Hypercomplex spectral signal representations for image processing and analysis*. PhD thesis, University of Kiel, Advisor-Gerald Sommer.

Bülow, T., & Sommer, G. (1997a). Das konzept einer zweidimensionalen phase unter verwendung einer algebraisch erweiterten signalrepräsentation. In *Mustererkennung, 1997, 19, DAGM-symposium* (pp. 351–358). London: Springer.

Bülow, T., & Sommer, G. (1997b). Multi-dimensional signal processing using an algebraically extended signal representation. In *AFPAC '97: Proceedings of the international workshop on algebraic frames for the perception-action cycle* (pp. 148–163). London: Springer.

Caselles, V., Catte, F., Coll, T., & Dibos, F. (1993). A geometric model for active contours in image processing. *Numerische Mathematik*, *66*, 1–31.

Caselles, V., Kimmel, R., & Sapiro, G. (1997). Geodesic active contours. *International Journal of Computer Vision*, *22*, 61–97.

Chan, T. F., Sandberg, B. Y., & Vese, L. A. (2000). Active contours without edges for vector-valued images. *Journal of Visual Communication and Image Representation*, *11*, 130–141.

Comaniciu, D., & Meer, P. (2002). Mean shift: a robust approach toward feature space analysis. *IEEE Transactions on Pattern Analysis and Machine Intelligence*, *24*(5), 603–619.

Cremers, D., Rousson, M., & Deriche, R. (2007). A review of statistical approaches to level set segmentation: integrating color, texture, motion and shape. *International Journal of Computer Vision*, *72*(2), 195–215.

Daugman, J. G. (1985). Uncertainty relation for resolution in space, spatial frequency, and orientation optimized by two-dimensional visual cortical filters. *Journal of the Optical Society of America A*, *2*(7), 1160–1169.

Delsuc, M. A. (1988). Spectral representation of 2D NMR spectra by hypercomplex numbers. *Journal of Magnetic Resonance*, *77*(1), 119–124.

Ell, T. (1993). Quaternion-Fourier transforms for analysis of two-dimensional linear time-invariant partial differential systems. In *Proceedings of the 32nd IEEE conference on decision and control* (Vol. 2, pp. 1830–1841).

Ell, T., & Sangwine, S. (2007). Hypercomplex Fourier transforms of color images. *IEEE Transactions on Image Processing*, *16*(1), 22–35.

Felzenszwalb, P. F., & Huttenlocher, D. P. (2004). Efficient graph-based image segmentation. *International Journal of Computer Vision*, *59*(2), 167–181.

Galatsanos, N. P., Wernic, M. N., Katsaggelos, A. K., & Molina, R. (2005). Multichannel image recovery. In A. Bovik (Ed.), *Handbook of image and video processing*. Amsterdam/San Diego: Elsevier/Academic Press.

Geman, S., & Geman, D. (1984). Stochastic relaxation, Gibbs distributions and the Bayesian restoration of images. *IEEE Transactions on Pattern Analysis and Machine Intelligence*, *6*(6), 721–741.

Herz, C. S. (1955). Bessel functions of matrix argument. *The Annals of Mathematics*, *61*(3), 474–523.

Hui, W., Xiao-Hui, W., Yue, Z., & Jie, Y. (2006). Color texture segmentation using quaternion-Garbor filters. In *IEEE international conference on image processing* (pp. 745–748).

Jian, B., & Vemuri, B. (2007a). Multi-fiber reconstruction from diffusion MRI using mixture of wisharts and sparse deconvolution. *Information Processing in Medical Imaging*, *20*, 384–395.

Jian, B., & Vemuri, B. C. (2007b). A unified computational framework for deconvolution to reconstruct multiple fibers from diffusion weighted MRI. *IEEE Transactions on Medical Imaging*, *26*(11), 1464–1471.

Jian, B., Vemuri, B. C., Özarslan, E., Carney, P., & Mareci, T. (2007). A novel tensor distribution model for the diffusion-weighted MR signal. *Neuroimage*, *37*(1), 164–176.

Kass, M., Witkin, A., & Terzopoulos, D. (1988). Snakes: active contour models. *International Journal of Computer Vision*, *1*(4), 321–331.

Kichenassamy, S., Kumar, A., Olver, P., Tannenbaum, A., & Yezzi, A. (1995). Gradient flows and geometric active contour models. In *IEEE international conference on computer vision* (pp. 810–815).

Kimmel, R., Malladi, R., & Sochen, N. A. (2000). Images as embedded maps and minimal surfaces: movies, color, texture, and volumetric medical images. *International Journal of Computer Vision*, *39*(2), 111–129.

Kuipers, J. B. (2002). *Quaternions and rotation sequences: a primer with applications to orbits, aerospace and virtual reality*. Princeton: Princeton University Press.

Lawson, C., & Hanson, R. J. (1974). *Solving least squares problems*. New York: Prentice-Hall.

Lukac, R., Smolka, B., Martin, K., Plataniotis, K., & Venetsanopoulos, A. (2005). Vector filtering for color imaging. *IEEE Signal Processing Magazine*, *22*(1), 74–86.

Malladi, R., Sethian, J. A., & Vemuri, B. C. (1995). Shape modeling with front propagation: a level set approach. *IEEE Transactions on Pattern Analysis and Machine Intelligence*, *17*(2), 158–175.

Mardia, K. V., & Jupp, P. E. (2000). *Directional statistics*, 2nd ed. New York: Wiley.

Martin, D., Fowlkes, C., Tal, D., & Malik, J. (2001). A database of human segmented natural images and its application to evaluating segmentation algorithms and measuring ecological statistics. In *IEEE international conference on computer vision* (Vol. 2, pp. 416–423).

Moxey, C., Sangwine, S., & Ell, T. (2003). Hypercomplex correlation techniques for vector images. *IEEE Transactions on Signal Processing*, *51*(7), 1941–1953.

Mumford, D., & Shah, J. (1985). Boundary detection by minimizing functionals. In *Proceedings of IEEE conference on computer vision and pattern recognition* (pp. 22–26).

Paragios, N., Chen, Y., & Faugeras, O. (2005). *Handbook of mathematical models in computer vision*. New York: Springer.

Pei, S.-C., & Cheng, C.-M. (1996). A novel block truncation coding of color images by using quaternion-moment-preserving principle. *IEEE International Symposium on Circuits and Systems*, *2*, 684–687.

Prentice, M. J. (1986). Orientation statistics without parametric assumptions. *Journal of the Royal Statistical Society. Series B (Methodological)*, *48*(2), 214–222.

Rousson, M., & Paragios, N. (2008). Prior knowledge, level set representations & visual grouping. *International Journal of Computer Vision*, *76*(3), 231–243.

Sangwine, S. (1996). Fourier transforms of colour images using quaternion or hypercomplex numbers. *Electronic Letters*, *32*(21), 1979–1980.

Sangwine, S. (1998). Colour image edge detector based on quaternion convolution. *Electronic Letters*, *34*(10), 969–971.

Sangwine, S., & Ell, T. A. (2000a). Colour image filters based on hypercomplex convolution. *IEE Proceedings on Vision, Image and Signal Processing*, *147*(2), 89–93.

Sangwine, S., & Ell, T. A. (2000b). The discrete Fourier transform of a colour image. In J. M. Blackledge & M. J. Turner (Eds.), *Image processing II: mathematical methods, algorithms and applications* (pp. 430–441).

Sapiro, G. (1997). Color snakes. *Computer Vision and Image Understanding*, *68*(2), 247–253.

Schoenemann, T., & Cremers, D. (2009). A combinatorial solution for model-based image segmentation and real-time tracking. *IEEE Transactions on Pattern Analysis and Machine Intelligence*, *99*(1).

Sethuraman, B. A., Rajan, B. S., Member, S., & Shashidhar, V. (2003). Full-diversity, highrate space-time block codes from division algebras. *IEEE Transactions on Information Theory*, *49*, 2596–2616.

Shi, L., & Funt, B. (2007). Quaternion color texture segmentation. *Computer Vision and Image Understanding*, *107*(1–2), 88–96.

Shoemake, K. (1985). Animating rotation with quaternion curves. In *SIGGRAPH'85: Proceedings of the 12th annual conference on computer graphics and interactive techniques* (pp. 245–254). New York: ACM.

Subakan, Ö. N., & Vemuri, B. C. (2008). Image segmentation via convolution of a level-set function with a Rigaut kernel. In *IEEE conference on computer vision and pattern recognition*, Anchorage, Alaska.

Subakan, Ö. N., Jian, B., Vemuri, B. C., & Vallejos, C. E. (2007). Feature preserving image smoothing using a continuous mixture of tensors. In *IEEE international conference on computer vision*, Rio de Janeiro, Brazil.

Tang, B., Sapiro, G., & Caselles, V. (2001). Color image enhancement via chromaticity diffusion. *IEEE Transactions on Image Processing*, *10*(5), 701–707.

Tsai, A., Yezzi, A. J., Wells, W. I., Tempany, C., Tucker, D., Fan, A., Grimson, W., & Willsky, A. (2001). Model-based curve evolution technique for image segmentation. In *IEEE conference on computer vision and pattern recognition* (Vol. 1, pp. 463–468).

Tschumperlé, D. (2006). Fast anisotropic smoothing of multi-valued images using curvature-preserving pde's. *International Journal of Computer Vision*, *68*(1), 65–82.

Tschumperlè, D. (2008). Greycstoration. Retrieved from http://cimg.sourceforge.net/greycstoration/, May 2008.

Weickert, J. (1997). Coherence-enhancing diffusion of colour images. In *7th national symposium on pattern recognition and image analysis* (pp. 239–244).

Zhu, S. C., & Yuille, A. (1996). Region competition: unifying snakes, region growing, and Bayes/MDL for multiband image segmentation. *IEEE Transactions on Pattern Analysis and Machine Intelligence*, *18*(9), 884–900.